AGU100 ADVANCING EARTH AND SPACE SCIENCE

JGR Earth Surface

RESEARCH ARTICLE
10.1029/2018JF004705

Key Points:
- We present Oligocene–Pliocene reconstructions of the bedrock topography of the Wilkes Subglacial Basin and Transantarctic Mountains
- Preglacial landscape of the Wilkes Subglacial Basin was situated close to sea level and governed in part by flexure and crustal structure
- Dynamic and oscillatory Oligocene–Miocene ice sheets drove enhanced bedrock erosion and associated flexural isostatic uplift

Supporting Information:
- Supporting Information S1

Correspondence to:
G. J. G. Paxman,
guy.j.paxman@durham.ac.uk

Citation:
Paxman, G. J. G., Jamieson, S. S. R., Ferraccioli, F., Bentley, M. J., Ross, N., Watts, A. B., et al. (2019). The role of lithospheric flexure in the landscape evolution of the Wilkes Subglacial Basin and Transantarctic Mountains, East Antarctica. *Journal of Geophysical Research: Earth Surface*, *124*, 812–829. https://doi.org/10.1029/2018JF004705

Received 26 APR 2018
Accepted 17 FEB 2019
Accepted article online 19 FEB 2019
Published online 19 MAR 2019

The Role of Lithospheric Flexure in the Landscape Evolution of the Wilkes Subglacial Basin and Transantarctic Mountains, East Antarctica

Guy J. G. Paxman[1], Stewart S. R. Jamieson[1], Fausto Ferraccioli[2], Michael J. Bentley[1], Neil Ross[3], Anthony B. Watts[4], German Leitchenkov[5,6], Egidio Armadillo[7], and Duncan A. Young[8]

[1]Department of Geography, Durham University, Durham, UK, [2]British Antarctic Survey, Cambridge, UK, [3]School of Geography, Politics and Sociology, Newcastle University, Newcastle upon Tyne, UK, [4]Department of Earth Sciences, Oxford University, Oxford, UK, [5]Institute for Geology and Mineral Resources of the World Ocean, St. Petersburg, Russia, [6]Institute of Earth Sciences, St. Petersburg State University, St. Petersburg, Russia, [7]Dipartimento di Scienze della Terra, dell'Ambiente e della Vita, Università di Genova, Genoa, Italy, [8]Institute for Geophysics, University of Texas, Austin, TX, USA

Abstract Reconstructions of the bedrock topography of Antarctica since the Eocene-Oligocene Boundary (approximately 34 Ma) provide important constraints for modeling Antarctic ice sheet evolution. This is particularly important in regions where the bedrock lies below sea level, since in these sectors the overlying ice sheet is thought to be most susceptible to past and future change. Here we use 3-D flexural modeling to reconstruct the evolution of the topography of the Wilkes Subglacial Basin (WSB) and Transantarctic Mountains (TAM) in East Antarctica. We estimate the spatial distribution of glacial erosion beneath the East Antarctic Ice Sheet, and restore this material to the topography, which is also adjusted for associated flexural isostatic responses. We independently constrain our post-34 Ma erosion estimates using offshore sediment stratigraphy interpretations. Our reconstructions provide a better-defined topographic boundary condition for modeling early East Antarctic Ice Sheet history. We show that the majority of glacial erosion and landscape evolution occurred prior to 14 Ma, which we interpret to reflect more dynamic and erosive early ice sheet behavior. In addition, we use closely spaced 2-D flexural models to test previously proposed hypotheses for a flexural origin of the TAM and WSB. The pre-34 Ma topography shows lateral variations along the length of the TAM and WSB that cannot be explained by uniform flexure along the front of the TAM. We show that some of these variations may be explained by additional flexural uplift along the south-western flank of the WSB and the Rennick Graben in northern Victoria Land.

1. Introduction

The Transantarctic Mountains (TAM) are a >3,000 km-long mountain range that separates East Antarctica and the West Antarctic Rift System (Figure 1). The peaks of the TAM protrude from beneath the East Antarctic Ice Sheet (EAIS) and rise to elevations >3 km above sea level. The Wilkes Subglacial Basin (WSB) is an extensive, low-lying region of the bedrock concealed beneath the EAIS in the hinterland of the TAM (Figure 1). Airborne radio-echo sounding (RES) surveys reveal that this sector of the EAIS is largely marine-based (grounded on bedrock that lies below sea level). These surveys show the WSB to be an ~1,400 km-long and 200 to 600 km-wide, south-to-north trending, subglacial depression, with bedrock elevations on average 500 m below sea level (Ferraccioli, Armadillo, Jordan, et al., 2009; Fretwell et al., 2013). The northern WSB contains deep sub-basins (up to 80 km wide), wherein the bed is situated up to 2.1 km below sea level; Ferraccioli, Armadillo, Jordan, et al., 2009; Jordan, Ferraccioli, Corr, et al., 2010; Figure 2).

The WSB is one of a number of large topographic basins that reach the coast of East Antarctica wherein large tracts of the EAIS are marine-based. This renders the ice sheet above the WSB potentially vulnerable to significant retreat in predicted future warmer climates (Pollard et al., 2015) as a result of marine ice sheet instability processes. Such processes have long been hypothesized for West Antarctica (Mercer, 1978; Schoof, 2007), but the importance of low-lying East Antarctic subglacial basins, which contain a much larger integrated volume of grounded ice (Fretwell et al., 2013), has only recently been more fully appreciated (Aitken et al., 2016; Bamber et al., 2009; DeConto & Pollard, 2016; Golledge et al., 2017; Mengel &

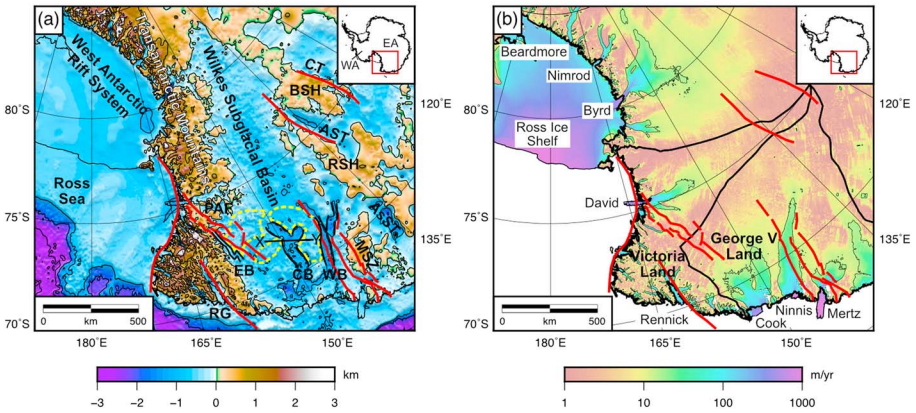

Figure 1. Regional setting of the Transantarctic Mountains and Wilkes Subglacial Basin within East Antarctica. (a) New digital elevation model of subglacial topography. Contour interval is 1 km, and elevations are relative to sea level. The red lines are proposed major crustal faults (Aitken et al., 2014; Cianfarra & Salvini, 2016; Ferraccioli, Armadillo, Jordan, et al., 2009; Ferraccioli & Bozzo, 2003; Jordan et al., 2013). The black lines denote outlines of sub-basins within the WSB (Ferraccioli, Armadillo, Jordan, et al., 2009). The yellow dashed lines mark the outline of flat bedrock plateaus (Paxman et al., 2018). Abbreviations: AST, Adventure Subglacial Trench; AsST, Astrolabe Subglacial Trench; BSH, Belgica Subglacial Highlands; CB, Central Basin; CT, Concordia Trench; EB, Eastern Basin; MSZ, Mertz Shear Zone; PAF, Prince Albert Fault; RG, Rennick Graben; RSH, Resolution Subglacial Highlands; WB, Western Basin. Inset shows the study area within Antarctica. EA, East Antarctica; WA, West Antarctica. (b) Ice surface velocity field (Rignot et al., 2011). The 25-m/year contour (thin black line) highlights regions of fast ice flow. The thick black lines represent major drainage basins (Rignot et al., 2013). Major outlet glaciers and ice shelves are labeled.

Levermann, 2014; Pollard et al., 2015). The northern WSB hosts the fast-flowing (velocities >25 m/year) Cook, Ninnis, and Mertz outlet glaciers, which together drain an EAIS catchment area of ~600,000 km^2, equating to ~5 m of eustatic sea level rise (Rignot et al., 2011).

Despite the importance of the WSB as a control on the future behavior of the EAIS, the topographic evolution of this region prior to and following EAIS inception at the Eocene–Oligocene transition (approximately 34 Ma) remains poorly understood (Gasson et al., 2015; Wilson et al., 2013). Unraveling the tectonic and

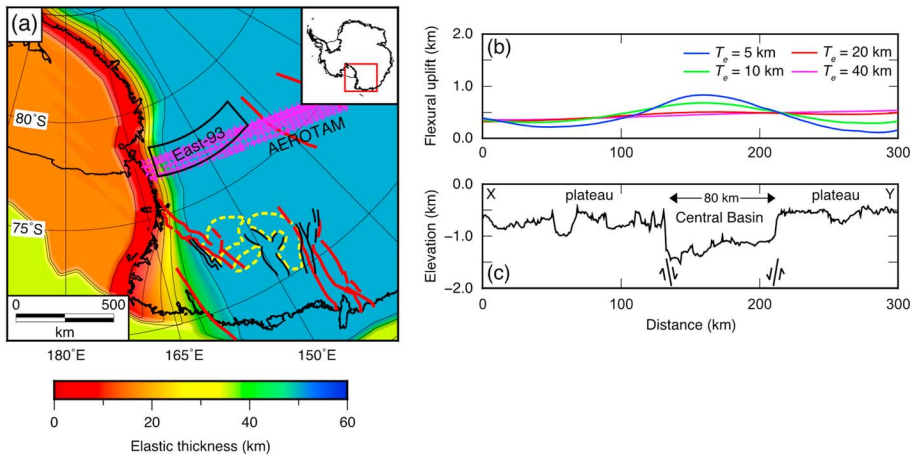

Figure 2. Effective elastic thickness model of the Transantarctic Mountains and Wilkes Subglacial Basin. (a) Grid of effective elastic thickness (T_e), consistent with forward topography and gravity models and spectral analysis (Chen et al., 2017; Close et al., 2009; ten Brink et al., 1997). The locations of the East-93 traverse and AEROTAM corridor survey, along which 2-D flexural and gravity modeling has previously been carried out (Studinger et al., 2004; ten Brink et al., 1997), are shown. The yellow dashed lines mark the outline of flat bedrock plateaus (Paxman et al., 2018). The red lines are major crustal faults. (b) Sensitivity of modeled flexural uplift due to incisional unloading (section 3.3) to the elastic thickness, T_e. The low-angle tilting associated with higher T_e values (>20 km) is consistent with the observed dip of the plateau surfaces. The sensitivity of the flexure to T_e value decreases with increasing T_e. (c) Modern-day bedrock topography along profile *X*-*Y* (location shown in Figure 1).

erosional evolution of the TAM and WSB will facilitate more accurate simulations of the behavior of past Antarctic ice sheets and in turn improve predictions of future ice sheet change under projected ocean and climate warming scenarios (DeConto & Pollard, 2016; Pollard et al., 2015).

2. Background and Aim

The mechanisms responsible for the formation and evolution of the WSB, and the closely associated TAM, remain subject to debate. A number of authors have interpreted the TAM as the uplifted flank of the West Antarctic Rift System, which is situated beneath the Ross Sea (Figure 1; Brenn et al., 2017; Hansen et al., 2016; Stern & ten Brink, 1989; ten Brink et al., 1997). The WSB is in turn interpreted as the product of flexural *back-bulge* subsidence induced by TAM uplift (Stern & ten Brink, 1989; ten Brink et al., 1997). This interpretation is supported by successful comparisons between 2-D flexural models and observed topographic profiles across the southern TAM and WSB (ten Brink et al., 1997). The magnitude and pattern of flexure is also constrained using apatite fission track thermochronology (Fitzgerald, 1992), and the observed westward dip of a Paleozoic erosion surface known as the Kukri Peneplain (Stern et al., 2005). Seismically derived crustal thickness estimates also lend support to a flexural origin for the TAM and WSB, indicating that the crust is of constant thickness and warps upward at the TAM and downward at the WSB (Hansen et al., 2016).

Early interpretations of thermochronology data indicated that the exhumation of the TAM occurred in three main stages during the Early Cretaceous, Late Cretaceous, and Cenozoic (Fitzgerald, 2002; Lisker, 2002). However, more recent evaluation of the thermochronology data, combined with thermal history modeling and the observed stratigraphic record, suggests that TAM uplift was spatially complex and diachronous along the mountain range rather than organized into three discrete events (Lisker et al., 2014; Lisker & Läufer, 2013). These thermochronology data indicate that the region was buried beneath a sedimentary basin during the Jurassic–Cretaceous, referred to as the Mesozoic Victoria Basin, which was removed by erosion following basin inversion and TAM uplift in the Paleogene (Lisker & Läufer, 2013; Prenzel et al., 2018). However, no deposits from this now-vanished basin have yet been described, and the uplift history of the TAM remains subject to ongoing debate.

Existing flexural models match (i) the observed height of the TAM, (ii) the width of the WSB, and (iii) geological constraints, if a free (broken) edge is assumed along the front of the TAM and the lithosphere of interior East Antarctica is assumed to be flexurally rigid (with an effective elastic thickness of ~85 km; Stern et al., 2005). However, 2-D flexural modeling has only been carried out along single profiles and narrow corridor surveys across the southern WSB and TAM (Studinger et al., 2004; ten Brink et al., 1997) and the effects of flexure have yet to be fully quantified in 3-D. It therefore remains unclear whether the flexure model is valid along the >1,000 km length of the TAM and WSB. Moreover, 3-D flexural modeling has shown that uplift driven by glacial valley incision within the central TAM—a process that was not incorporated into the original 2-D models—can account for between 32% and 50% of the observed peak elevations (Stern et al., 2005). The role of erosion-driven uplift in the WSB has yet to be quantified, in contrast to the Recovery basin, where quantitative modeling has demonstrated that glacial erosion and flexure have, in combination, driven substantial relief generation (Paxman et al., 2017).

Other workers have proposed that the geometry of the WSB is structurally controlled in light of potential field and ice-penetrating radar data sets, which reveal that the WSB is fault-bounded and appears to follow the geometry of the underlying tectonic architecture in the basement (Figure 1; Aitken et al., 2014; Chiappini et al., 2002; Ferraccioli, Armadillo, Zunino, et al., 2009; Ferraccioli & Bozzo, 2003; Jordan et al., 2013). Aeromagnetic interpretations also indicate the presence of Jurassic tholeiites and post-Jurassic graben-like features within the WSB (Ferraccioli, Armadillo, Jordan, et al., 2009). However, there are no high-amplitude magnetic anomalies in the WSB comparable to those observed over Cenozoic rift related rocks over the adjacent TAM or within the West Antarctic Rift System (Ferraccioli, Armadillo, Zunino, et al., 2009). Based on aeromagnetic and airborne gravity data interpretations, crustal extension associated with a Ross-age (approximately 500 Ma) back-arc setting and Jurassic–Cretaceous Gondwana breakup has been proposed to have affected the basement of the WSB (Ferraccioli, Armadillo, Jordan, et al., 2009; Jordan et al., 2013). However, passive seismic data arrays currently only sample the eastern edge of the basin and these observations do not reveal large-scale crustal thinning beneath the WSB, but rather a marginally thicker crust with

respect to the adjacent TAM (An et al., 2015; Hansen et al., 2016). Overall, the influence of the inherited basement architecture on the evolution of the modern topography of the WSB remains unclear.

The aim of this study is twofold. First, we aim to reconstruct the paleotopography of the TAM and WSB from 34 Ma to present by estimating the spatial distribution of glacial erosion and using 3-D flexural modeling to determine the associated flexural response. Using our new reconstruction of 34 Ma topography, we then aim to use 2-D flexural models to reevaluate previously published hypotheses that invoke a flexural origin of the TAM and WSB (Stern & ten Brink, 1989; ten Brink et al., 1997) in light of more recently acquired radar data sets, and in so doing assess the role of lithospheric flexure in shaping the topography along the full length of the TAM-WSB system prior and subsequent to EAIS inception.

3. Methods

3.1. Bedrock Elevation Gridding

This study uses RES data sets acquired during a number of airborne geophysical campaigns over the previous two decades. During RES surveys, ice-penetrating radar waves are reflected at the ice-bed interface; the two-way travel time of the bed echo, combined with the velocity of radar in ice, is used to calculate the ice thickness, from which the bedrock elevation can be computed. We combined over 200,000 line-kilometer of radar data from the WISE-ISODYN (Wilkes Basin/Transantarctic Mountains System Exploration - Icehouse Earth: Stability Or Dynamism?; Ferraccioli, Armadillo, Jordan, et al., 2009; Ferraccioli, Armadillo, Zunino, et al., 2009; Jordan et al., 2013; Jordan, Ferraccioli, Corr, et al., 2010), ICECAP (International Collaborative Exploration of the Cryosphere through Airborne Profiling; Blankenship et al., 2017), Operation IceBridge (Leuschen et al., 2016), and AEROTAM (Studinger et al., 2004) surveys (Figure S1 in the supporting information).

The bedrock elevation line data were initially referenced to the WGS84 ellipsoid. We applied an ellipsoid-geoid conversion to reference the elevations to mean sea level, matching the Bedmap2 compilation (Fretwell et al., 2013). We then interpolated the bedrock elevation data onto a 2 km grid mesh using a continuous curvature spline algorithm (Wessel et al., 2013) with a tension factor of 0.35. The resulting bedrock topography digital elevation model (DEM) was masked to remove any interpolated values more than 10 km from the nearest data point (Figure S1), and these empty nodes were replaced with bedrock elevation values from the Bedmap2 compilation (Fretwell et al., 2013), which includes data from other sources including rock outcrop elevations and thin-ice models over the TAM. The DEM (Figure 1a) forms the basis for our estimation of bedrock erosion and 3-D flexural modeling used to reconstruct paleotopography.

3.2. Effective Elastic Thickness Grid

In order to quantify flexural uplift within the TAM and WSB, we employed 2-D and 3-D elastic plate flexure models (see e.g., section 3.3). The free parameter in these models is the effective elastic thickness of the lithosphere, T_e, which is a proxy for the depth-integrated strength of the lithosphere. We set up a simple T_e model for the TAM, WSB, and surrounding regions based on existing constraints.

Forward and inverse (spectral) modeling suggests that T_e increases from 5 km at the front of the TAM to high values in interior East Antarctica (Chen et al., 2017; Ji et al., 2017; ten Brink et al., 1997). However, the exact value of this *high* T_e varies between different methods. Forward models require T_e values of up to 85 km under the southern WSB in order to match the observed long-wavelength and low amplitude downward of the basin (Stern et al., 2005; ten Brink et al., 1997). However, this estimate was determined using a single 2-D model across the southern TAM and WSB (Figure 2) and does not account for any lateral variation along the mountain range or basin. Inverse spectral methods (gravitational admittance and coherence) indicate that T_e increases from ~30 to ~60 km westward across the WSB (Chen et al., 2017; Ji et al., 2017).

Constraints on the regional T_e can also be garnered from smaller scale features of the landscape. For example, the fault-bounded Eastern, Central, and Western Basins within the WSB are likely to have been the locus erosional and mechanical unloading within the WSB and are separated by extensive, flat-lying plateaus (Paxman et al., 2018). The absence of short-wavelength tilting of the flanking plateau regions is therefore indicative of relatively high regional T_e values (>20 km) within the WSB (Figure 2).

We assumed a T_e of 15 km for the Ross Sea, reflecting the relatively weak lithosphere underlying the West Antarctic Rift System (Chen et al., 2017; Ji et al., 2017; Jordan, Ferraccioli, Vaughan, et al., 2010; Stern & ten Brink, 1989). T_e was then increased from 5 km at the TAM front to 50 km in the interior of East Antarctica, which reflects an average of the values recovered using forward and inverse modeling techniques. T_e is smoothly graded across the continental margin to 35 km, reflecting values reported for the oceanic lithosphere beyond the continental slope (Close et al., 2009). This spatially variable T_e model (Figure 2) was used in our 3-D flexural models (section 3.3). However, given the range of reported T_e values for the TAM and WSB, we carried out sensitivity testing to evaluate the effect of different T_e scenarios on the modeled flexure (Figure S2).

3.3. Valley Incisional Unloading

Removal of material from Earth's surface by glacial and/or fluvial erosion causes unloading of the lithosphere. Consequently, buoyancy forces from the mantle and elastic bending forces within the lithosphere drive isostatic uplift of the Earth's surface (Watts, 2001). Because the lithosphere has a finite flexural rigidity, isostatic uplift is distributed over a wider horizontal extent than the localized incision (Figure 2c). Areas that are not eroded therefore experience net surface uplift, even though the average elevation of the region will decrease (Molnar & England, 1990).

In order to estimate the 3-D distribution of glacial incision within the TAM and WSB, the bedrock DEM was first rebounded for the removal of the modern ice sheet load (Figure 3). To estimate the spatial distribution of erosion, we used RES profiles and the DEM to identify bedrock peaks interpreted as remnants of a preglacial landscape. We then interpolated a smooth continuous surface between these summits, which are assumed to have not experienced significant erosion since EAIS inception at 34 Ma. This summit accordance surface is therefore a reconstruction of the preerosion landscape and represents the restoration of eroded material to the topography without accounting for the associated isostatic response (Champagnac et al., 2007; Stern et al., 2005). The difference between the summit accordance surface and the ice-free bedrock topography represents our estimate of glacial incision (Figure 3).

The flexural response of the lithosphere to ice loading and valley incision was computed using an isostatic model that calculates the flexural adjustment (w) to loading (h) of a thin elastic plate overlying an inviscid fluid (Watts, 2001)

$$\nabla^2\left[D(x,y)\nabla^2 w(x,y)\right] + (\rho_{\text{mantle}} - \rho_{\text{infill}})gw(x,y) = \left(\rho_{\text{load}} - \rho_{\text{displace}}\right)gh(x,y) \tag{1}$$

where

$$D(x,y) = \frac{\text{ET}_\text{e}(x,y)^3}{12(1-\nu^2)} \tag{2}$$

is the flexural rigidity of the lithosphere as a function of spatial dimensions x and y. E (Young's modulus; 100 GPa) and ν (Poisson's ratio; 0.25) are elastic constants, and the density terms (ρ) depend on the particular loading or unloading situation being considered. Equation (1) was solved numerically using a centered finite difference technique, with the T_e scenario as shown in Figure 2. For ice loading we assumed a load density of 915 kg/m^3, and for erosional unloading a density of 2,500 kg/m^3, reflecting Beacon Supergroup sediments and Ferrar dolerites (Ferraccioli, Armadillo, Jordan, et al., 2009). Densities of 3,330 kg/m^3 were assumed for the mantle and 0 kg/m^3 for the material infilling (and displaced by) the flexure. We evaluated the flexure outputs from our numerical model by comparison with analytical solutions (Figure S3).

As well as valley incision into basement, material may also have been removed from the TAM and WSB by the initial downwearing of the terrestrial deposits of the Mesozoic Victoria Basin (Lisker & Läufer, 2013; Prenzel et al., 2018). However, aside from at geographically confined localities in the TAM, the paleo-thickness of these deposits, and the amount removed by erosion after 34 Ma across the study area, is unconstrained. As a result, it is difficult to model the effects of the removal of any preexisting sedimentary overburden. We therefore assumed a simplistic geometry of the possible eroded overburden based on largely qualitative scenarios proposed by previous authors (Prenzel et al., 2018; Figure S4). We computed the flexural response to the erosion of this sedimentary basin assuming a load density of 2,350 kg/m^3 to

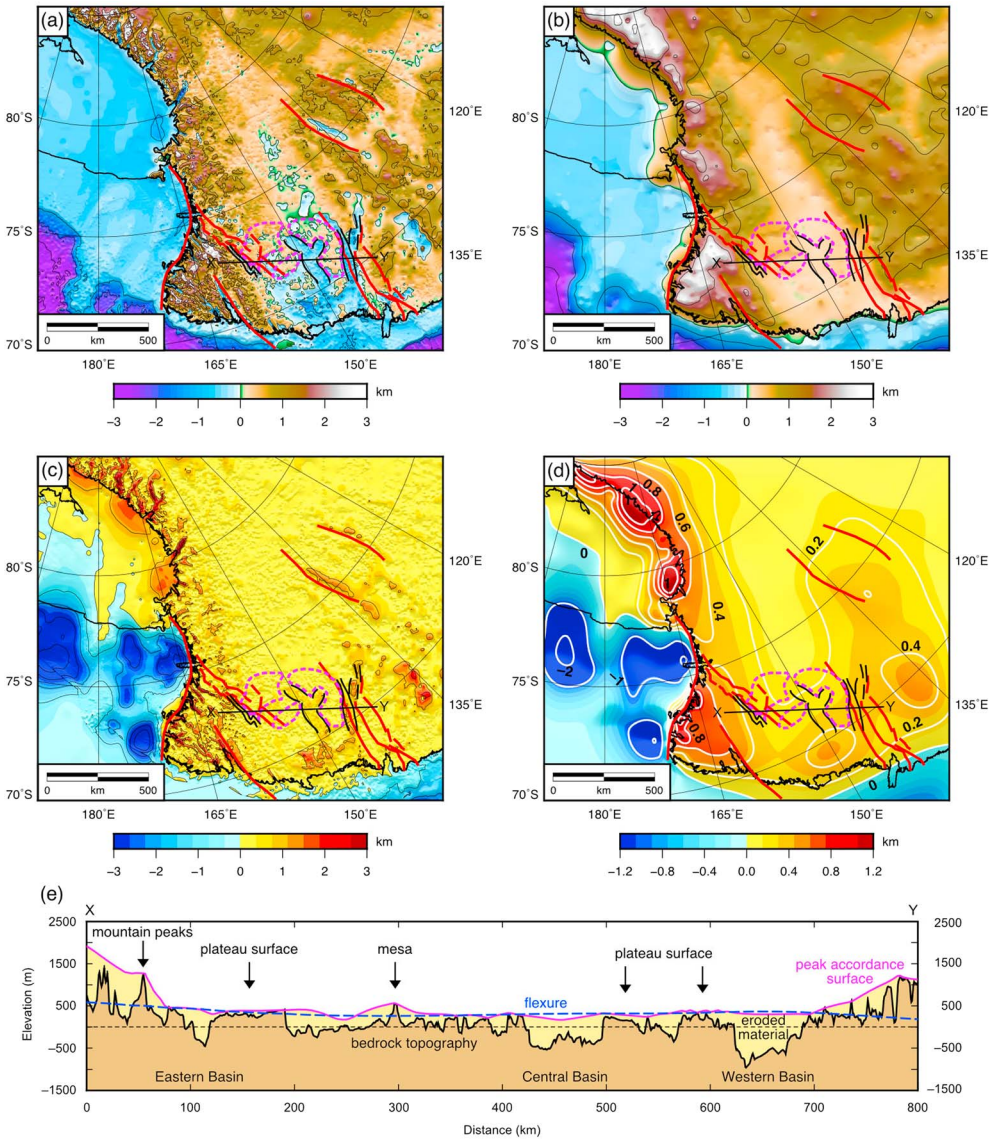

Figure 3. Isostatic response to valley incision and sediment loading. (a) Topography adjusted for removal of modern ice load. The red lines are major crustal faults (Aitken et al., 2014; Cianfarra & Salvini, 2016; Ferraccioli & Bozzo, 2003); the black lines show sub-basin outlines (Ferraccioli, Armadillo, Jordan, et al., 2009); the dashed magenta lines mark the outline of flat bedrock plateaus (Paxman et al., 2018). (b) Peak accordance surface. (c) Eroded material (warm colors), computed by subtracting the rebounded topography (panel a) from the peak accordance surface (panel b). Offshore sediment (cool colors) 34–0 Ma in age derived from seismic sediment thickness data sets. (d) Cumulative flexural response to incisional unloading (warm colors) and sediment loading (cool colors) since 34 Ma. Contour interval is 0.2 km onshore and 1 km offshore, and selected contours are labeled in kilometers. (e) Profile *X*–*Y* crossing the northern Wilkes Subglacial Basin (location show in panels a–d). Bedrock topography is adjusted for ice sheet loading. The summit accordance surface joins mountain peaks, mesas, and plateaus, which are all assumed to have experienced negligible glacial (post-34 Ma) erosion. The thickness of eroded material is the difference between the accordance surface and the bedrock topography.

reflect the proposed unconsolidated nature of the deposits (Figure S4; Lisker & Läufer, 2013; Prenzel et al., 2018).

3.4. Offshore Sediment Thickness

The distribution of sediment located on the continental shelf was used to (1) calculate the flexural response to sediment loading since 34 Ma and (2) compare the mass of offshore sediment to the estimated mass of eroded material in order to assess whether this estimate is realistic. The glacially eroded material (Figure 3c) was likely routed through the TAM or northern margin of the WSB and deposited in offshore

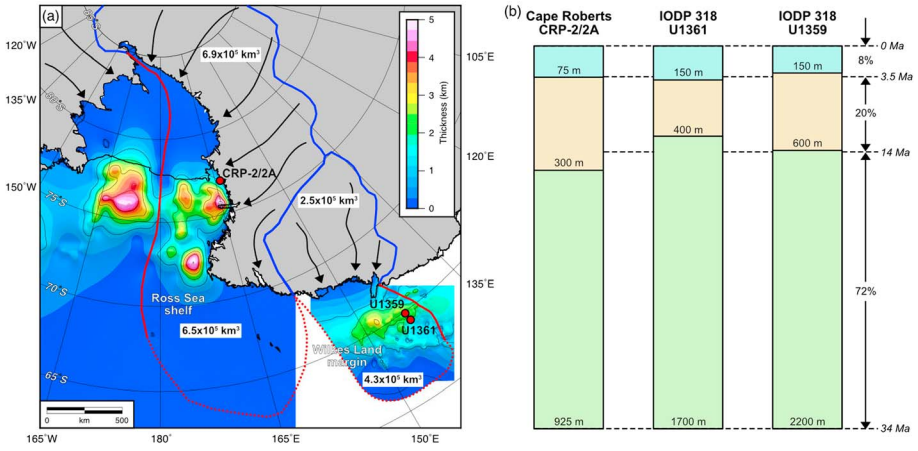

Figure 4. Comparison of volumes of erosion and sediment. (a) Offshore sediment isopachs indicate the thickness of sediment determined from seismic reflection surveys (Lindeque et al., 2016). The red lines show mapped (solid) and inferred (dashed) sediment provenance boundaries for material routed through the Transantarctic Mountains into the Ross Sea, and through the Wilkes Subglacial Basin onto the Wilkes Land margin (Cook et al., 2013; Naish et al., 2009; Zattin et al., 2012). The blue lines denote divides between ice sheet catchments, which govern the direction of transport of eroded material (black arrows; Rignot et al., 2011). Volumes of eroded material and offshore sediment within the different catchments are shown. (b) Schematic sediment columns based on ocean sediment drill cores and seismic reflection profiles in the Ross Sea and Wilkes Land (locations shown by red circles in panel a; Escutia et al., 2011; Lindeque et al., 2016; Naish et al., 2001). Down-core depths of the boundaries between sediment packages (34–14 Ma, 14–3.5 Ma, and 3.5–0 Ma) are labeled.

basins on the Ross Sea shelf and Wilkes Land margin (Figure 4), although some may have been deposited in onshore depocenters (Jamieson et al., 2014). We used glacial (34–0 Ma) sediment thickness grids for the Ross Sea shelf (Lindeque et al., 2016) and the Wilkes Land margin northward of the mouth of the WSB (Paxman et al., 2018; Figure 4).

3.4.1. Flexure Due to Sediment Loading

Sediment loading offshore has the potential to cause bedrock subsidence offshore and uplift onshore. Our elastic plate model (equation (1)) was used to compute the flexural response to sediment loading, assuming an average sediment (load) density of 2,200 kg/m^3 (Wilson et al., 2012) and infill and displacement densities of 1,030 kg/m^3 to represent seawater. The resulting flexural response was combined with the flexural uplift due to valley incision into a complete grid of flexural isostatic adjustment (Figure 3d).

Our models do not explicitly take into account onshore sediment loading since 34 Ma. Although magnetic depth-to-source modeling (Frederick et al., 2016) and spectral roughness calculations (Siegert et al., 2005) indicate a significant coverage of sediment within the WSB, potential field modeling indicates that the majority of this sediment is likely composed of Beacon Supergroup strata (Devonian–Triassic) or Neoproterozoic metasedimentary rocks and that negligible (<1 km) Cenozoic sediments are preserved within the basin (Ferraccioli, Armadillo, Jordan, et al., 2009; Studinger et al., 2004). Because the summit accordance method (section 3.3) estimates the net amount of onshore erosion (i.e., the difference between erosion and sedimentation), any replacement of eroded bedrock by deposited sediment within the deep onshore basins of the WSB is implicitly incorporated into our models.

3.4.2. Mass Balance of Sediment and Eroded Material

The volume of eroded material (Figure 3c) was compared to the volume of offshore sediment (Figure 4). We divided the eroded material into two fractions—(1) material derived from the TAM and southern WSB, routed through the valleys of the TAM and deposited on the Ross Sea shelf, and (2) material eroded from within the subglacial troughs of the northern WSB and routed to the Wilkes Land margin via the George V Coast (Figure 4). To make this division, we assumed that eroded material has consistently followed the modern-day flow-lines of the EAIS and cannot cross the major drainage divides (Rignot et al., 2011; Figure 4). The location of the corresponding offshore sediment was established using offshore sediment provenance studies (Cook et al., 2013; Zattin et al., 2012; Figure 4). The volume of eroded material was converted to a mass assuming an average density of 2,500 kg/m^3, reflecting a realistic average of Beacon Supergroup

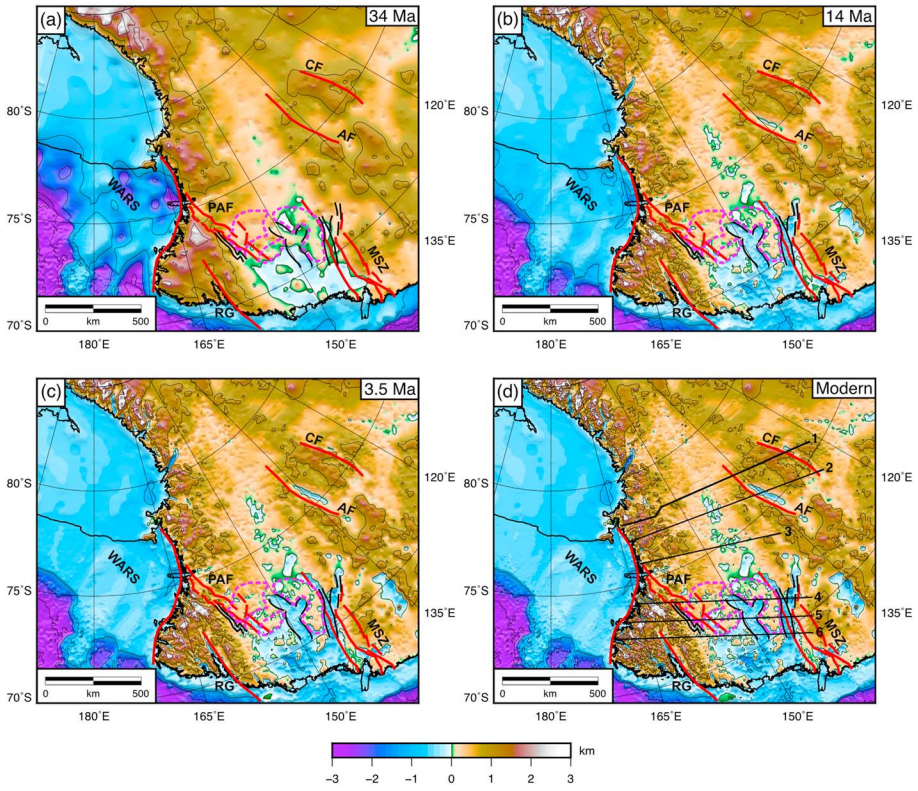

Figure 5. Regional paleotopography from 34 Ma to present. (a) Bedrock topography at the Eocene-Oligocene boundary (34 Ma). The red lines are major crustal faults (Aitken et al., 2014; Cianfarra & Salvini, 2016; Ferraccioli & Bozzo, 2003); the black lines show sub-basin outlines (Ferraccioli, Armadillo, Jordan, et al., 2009); the dashed magenta lines mark the extent of flat bedrock plateaus (Paxman et al., 2018). Abbreviations: AF, Adventure Fault; CF, Concordia Fault; MSZ, Mertz Shear Zone; PAF, Prince Albert Fault; RG, Rennick Graben; WARS, West Antarctic Rift System. (b) Bedrock topography at the mid-Miocene climatic optimum (approximately 14 ma). (c) Bedrock topography during the mid-Pliocene warm period (approximately 3.5 ma). (d) Modern bedrock topography. All elevations are relative to the geoid (present-day sea level) in the absence of any ice loading. The black lines indicate flight paths of the radio-echo sounding lines used for our six 2-D flexural models (Figure 6). Radio-echo sounding lines were obtained from the ICECAP (1), AEROTAM (2), and WISE-ISODYN (3–6) surveys (survey flight/line names are indicated in Figure 6).

sedimentary rocks, Ferrar dolerites, and younger sediments. The mass of offshore sediment was computed using a density of 2,200 kg/m^3 and accounting for typical fractions (5–15%) of biogenic (nondetrital) material within the offshore sediment (Wilson et al., 2012).

3.5. Paleotopography Model: 34 Ma to Present

We followed a series of steps to produce an estimate of paleotopography for 34 Ma:

1. Adjust the modern bedrock topography (Figure 2a) for the removal of the modern ice sheet load (section 3.3 and Figure 3a).
2. Remove the 34 to 0 Ma sediment from the continental shelf and add the eroded material to the land surface (Figure 3c).
3. Subtract the flexural isostatic response to sediment loading and incisional unloading (Figure 3d).
4. Gaussian filter at 10 km resolution to remove short-wavelength artifacts introduced by the reconstruction process.

The resulting reconstruction of 34 Ma bedrock topography (Figure 5), from which the effects of (post-34 Ma) ice loading, incisional unloading, and sediment loading have been removed, is hereafter referred to as the *residual topography*. We note while that the paleobathymetry of the Ross Sea is shown for completeness (Figure 5), this has been influenced by extension and subsidence within the West Antarctic Rift System (Wilson et al., 2012), which is not accounted for in our models.

In order to produce a continuous model of the evolution of bedrock topography from 34 Ma to present, an approximate temporal history of sediment deposition was established. We used existing offshore sediment thickness data from drill cores on the Wilkes Land margin (Escutia et al., 2011; Tauxe et al., 2012) and in the western Ross Sea (Naish et al., 2001). Using three separate drill cores, we established the thickness of offshore sediment deposited between key climate transitions—the Eocene–Oligocene transition (approximately 34 Ma), mid-Miocene climatic optimum (approximately 14 Ma), and mid-Pliocene warm period (approximately 3.5 Ma; Figure 4). Assuming that the rate of sedimentation is a direct proxy for the rate of onshore erosion, these thicknesses provide a chronology for the rate of erosion and flexure since 34 Ma and enable us to produce reconstructions of paleotopography at the times of these key climate transitions (Figure 5). An important caveat is the presence of unconformities in the sedimentary records (Escutia et al., 2011), which indicate that material has been periodically removed from the shelf. Since it is unclear how much shelf material has been removed, apparent sedimentation rates may not be directly correlated to 'true' onshore erosion rates.

3.6. Two-Dimensional Flexural Modeling of TAM Uplift and WSB Subsidence

The original models for the preglacial evolution of the TAM and WSB invoke broad flexure of the East Antarctic lithosphere (section 2; Stern & ten Brink, 1989; ten Brink et al., 1997). We reappraise these models along the length of the TAM and WSB using more recent ice thickness and bedrock elevation constraints (Figure 1), which have been adjusted for the effects of ice loading, valley incision, and sediment loading (Figure 5). We model the topography along six 700 to 1,100 km-long RES profiles that extend from the Ross Sea coast across the TAM and WSB into the interior of East Antarctica (Figures 6 and 7). The six profiles are approximately evenly spaced and span an ~1,000 km length of the TAM and WSB, thereby significantly expanding the coverage of the early models of ten Brink et al. (1997). In order to reevaluate these previous studies (Lawrence et al., 2006; ten Brink et al., 1997), we incorporate into our flexural model the following loading mechanisms:

1. A buoyant erosional unload associated with denudation at the front of the TAM.
2. A buoyant thermal load due to conduction of heat from West Antarctica to East Antarctica.
3. An *isostatic end load*, which is required to match the amplitude of rock uplift at the edge of the TAM. This simplified load represents mechanical unloading due to lithospheric thinning and extension within the Ross Sea (Stern & ten Brink, 1989).

The geometry of the modeled loads is shown in Figure S5. We employed the T_e model used by ten Brink et al. (1997), with a single plate break along the length of the TAM and T_e linearly increasing from 5 km at the TAM front to a constant *high* value at a distance of 130 km inland. The modeled topography was compared to the residual topography along the six RES profiles (Figure 6). We carried out sensitivity testing by varying the high value of T_e assumed for the WSB, in order to determine whether there existed a range of T_e values for which the flexure model could (or could not) satisfactorily account for the observed topography (Figure S6).

Where this first-order model could not explain features of the residual topography, we incorporated the effects of other major crustal faults (Figure 7). We incorporated fault locations that have been independently mapped in this region using geological data, magnetic lineaments, gravity anomalies, ice surface lineaments, and bedrock topography profiles (Aitken et al., 2014; Cianfarra & Salvini, 2014; Ferraccioli, Armadillo, Jordan, et al., 2009, 2013; Scheinert et al., 2016). We modeled these faults as drivers of uplift along their flanks due to mechanical unloading of the lithosphere during extensional faulting and concomitant flexural rebound (Watts, 2001; Weissel & Karner, 1989). In order to compute this flexural response, we used our standard T_e model (Figure 2) and assumed a crustal thickness of 40 km, and crust and mantle densities of 2,800 and 3,330 kg/m^3, respectively. Each fault was assumed to dip at 60° toward the downthrown side. The amount of cumulative displacement across the faults was tuned to match the amplitude of the adjacent topography. We experimented with a series of combinations of increasing complexity and computed the root-mean-square misfit between residual and modeled topography to determine the most parsimonious model that could adequately account for the observed large-scale geometry of the TAM and WSB by minimizing the misfit (Figure 6). Since there was likely some inherited topography prior to flexural warping (ten Brink et al., 1997), we focus on the long-wavelength patterns of uplift as well as the absolute elevations.

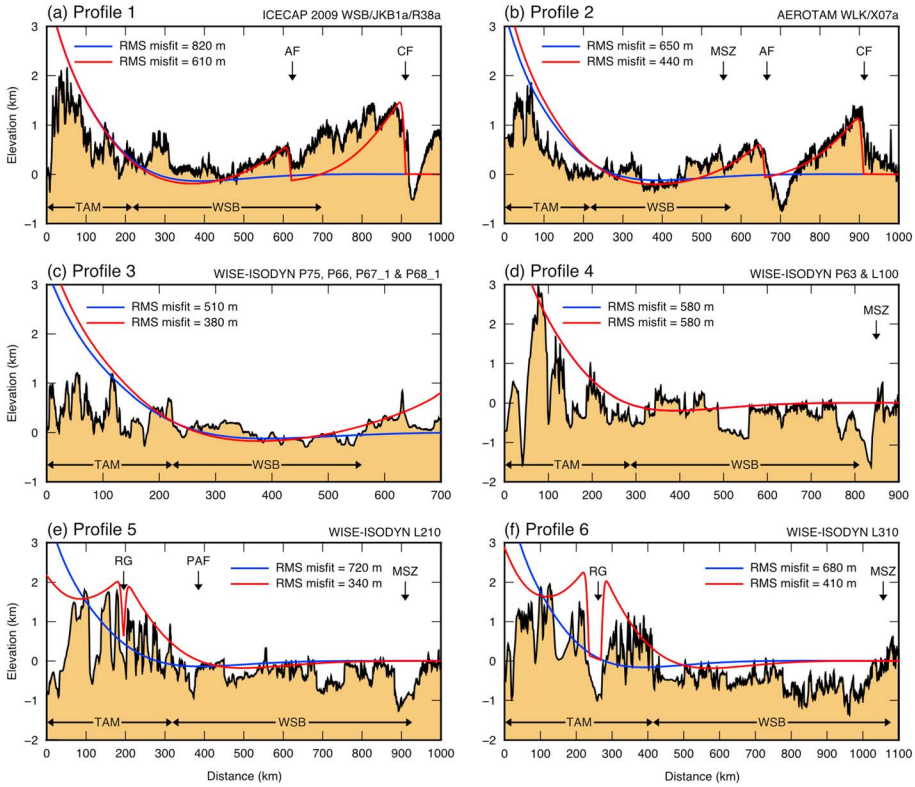

Figure 6. 2-D flexural models along six radar profiles crossing the Transantarctic Mountains and Wilkes Subglacial Basin. (a–f) Profile locations (1–6) are displayed in Figures 5 and 7. The names of the lines, as given in the individual geophysical surveys, are provided. The bedrock is shown by the black line and shaded region. Bed elevations have been adjusted for the effects of ice sheet loading, incisional unloading, and sediment loading. The eroded material has not been filled in so as to retain the clarity of the original topography. Our models therefore attempt to match the elevations of the peaks, which are assumed not to have been eroded. The blue line shows the original flexural model of ten Brink et al. (1997), with a single plate break along the front of the Transantarctic Mountains. The red line shows the best fitting model in this study; flexural uplift due to mechanical unloading along other faults (labeled with black arrows) is incorporated. The root-mean-square (RMS) misfits between the residual and modeled peak elevations for each model are quoted in each panel. Abbreviations: AF, Adventure Fault; CF, Concordia Fault; MSZ, Mertz Shear Zone; PAF, Prince Albert Fault; RG, Rennick Graben.

4. Results

The bedrock DEM shows that the northern WSB contains deep sub-basins (up to 80 km wide and 2.1 km below sea level) that extend over 300 km inland from the grounding line (Ferraccioli, Armadillo, Jordan, et al., 2009; Jordan, Ferraccioli, Vaughan, et al., 2010; Figure 2). These deep basins are superimposed on pre-existing tectonic features (Ferraccioli, Armadillo, Jordan, et al., 2009; Jordan et al., 2013) and are separated by elevated, flat-lying, dissected plateau surfaces that are interpreted as remnants of a widespread low-lying erosion surface (Paxman et al., 2018). The WSB also contains smaller scale flat-topped bedrock highs, which resemble mesas or buttes (Studinger et al., 2004). The peaks of the TAM rise to >3 km above sea level and have been incised by deep glacial valleys, the floors of which are in places more than 2 km below sea level (Figure 2). The peaks of the TAM (Stern et al., 2005), bedrock plateau surfaces within the northern WSB, and smaller scale mesas and buttes were used to reconstruct the *pre-incision* landscape of the TAM and WSB and estimate the distribution of glacial erosion (section 3.3). In total, we estimate that ~10^6 km^3 (~2×10^{18} kg) of material has been removed from the region by glacial valley incision since 34 Ma. More than 1 km of material has been removed from the deep glacial troughs within the northern WSB and >3 km of erosion has occurred within some of the deep valleys that cut through the TAM (Figures 3c and S7).

Removal of this material has driven 600–900 m of flexural uplift along the front of the TAM, which on average accounts for approximately one third of the present-day elevation of the mountain peaks (Figure 3d). In parts of the central and southern TAM, flexure accounts for up to 40–50% of the observed peak elevations,

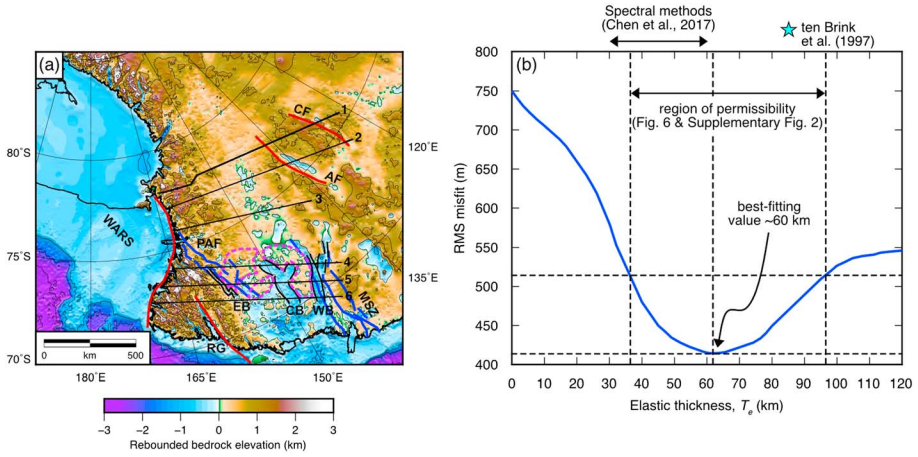

Figure 7. Elastic plate modeling results. (a) Present-day bedrock elevation (rebounded for ice sheet loading). The black lines indicate flight paths of the radio-echo sounding lines used for our six 2-D flexural models (Figure 6). The red lines show major faults along which plate breaks and motion are modeled to account for the geometry of the Transantarctic Mountains and Wilkes Subglacial Basin. The blue lines show additional faults, which influence the regional structure and topographic geometry (Aitken et al., 2014), but do not have significant flexural effects. The black lines show sub-basin outlines (Ferraccioli, Armadillo, Jordan, et al., 2009); the dashed magenta lines mark the extent of flat bedrock plateaus (Paxman et al., 2018). Abbreviations: AF, Adventure Fault; CF, Concordia Fault; MSZ, Mertz Shear Zone; PAF, Prince Albert Fault; RG, Rennick Graben; WARS, West Antarctic Rift System. (b) Root-mean-square misfit between the residual topography and the flexurally modeled topography (Figure 6) as a function of the effective elastic thickness, T_e, assumed beneath the Wilkes Subglacial Basin. The gridlines indicate the best fit average elastic thickness and band of <100 m greater than the minimum root-mean-square, used to define a region of permissibility. Estimates of T_e from previous studies are shown for context.

supporting the findings of previous modeling (Stern et al., 2005). In the northern WSB, flexure has driven 200–300 m of uplift (Figure 3d), which is broadly distributed owing to the high flexural rigidity of the underlying lithosphere (Figure 2). Sensitivity testing indicates that the magnitude of flexural uplift in the WSB does not vary significantly (<200 m) for a realistic range of T_e values (Figure S2). At 34 Ma, the relief within the northern WSB was much less dramatic that at the present day, because the sub-basins were significantly shallower prior to being glacially overdeepened (Figure 5).

The volume of material eroded by incision within the subglacial troughs of the WSB and subsequently routed through the George V Coast is 2.5×10^5 km^3, which compares well to the volume of post-34 Ma sediment on the Wilkes Land margin: 4.3×10^5 km^3. These values correspond to masses of 0.63 Pt (Petatonnes; 10^{18} kg) of eroded material and 0.80–0.90 Pt of shelf sediment. The volume of material eroded from TAM and southern WSB is 6.9×10^5 km^3 (1.7 Pt), and the volume of post-34 Ma sediment on the Ross Sea shelf is 6.5×10^5 km^3 (1.1–1.3 Pt). Offshore sediment cores (Figure 4) show that, on average, 72% of the glacial (post-34 Ma) sediment had been deposited by 14 Ma, and 92% by 3.5 Ma, and sedimentation rates were approximately constant between these time slices.

Although uncertainties propagate in the erosion model and in the seismic sediment isopachs, as well as the unknown amount of material lost from the shelf due to reworking by ocean currents, the volumes and masses of offshore sediment and eroded material agree to within a factor of 2. This result indicates that our erosion model is realistic to first order and that it is unlikely that large volumes of post-34 Ma sediment are situated in onshore depocenters. We encapsulate the ± ~50% uncertainty in our erosion/sedimentation estimate, as well as the uncertainty associated with the regional T_e used to determine the associated flexural responses (Figure S2), by producing minimum and maximum reconstructions of the paleotopography at each time slice (Figure S8).

The volumes and masses given above do not include the possible extra thickness of eroded material due to the downwearing of the Mesozoic Victoria Basin (section 3.3). The simple basin thickness scenario shown in Figure S4 contains 3.90 Pt of material. The notably smaller observed mass of post-34 Ma offshore sediment (1.90–2.20 Pt, most of which can be accounted for by the estimated valley incision) indicates that if such thicknesses of terrestrial sediment were deposited in the Mesozoic Victoria Basin, they were largely eroded

prior to approximately 34 Ma. Alternatively, the sequence may have been much thinner and/or more restricted than the scenario in Figure S4. Because of the uncertainty regarding the amount of Mesozoic Victoria Basin overburden removed after 34 Ma, and because thermochronology data indicate that this downwearing occurred over a short space of time (approximately 5 Myr; Prenzel et al., 2018), we restore the overburden to the only the maximum topography for the Eocene-Oligocene Boundary as a possible end-member scenario (Figure S8). We do however note the potentially important implications of now-vanished sedimentary basins for Cenozoic paleotopography and highlight the necessity for more sophisticated basin modeling techniques and improved constraints in order to fully understand the consequences for topographic reconstructions.

Our 2-D flexural modeling results show that the model of ten Brink et al. (1997) can account for the width and amplitude of the TAM at the southern end of the study area (Figures 6a and 6b). However, this simple one-dimensional model fails to account for a number of first-order observations of the geometry of the residual topography. First, it fails to account for the upwarping of the topography in the southwest of the WSB, where the basin takes on an approximately symmetrical profile, which cannot be explained by a flexural model in which unloading is entirely concentrated at the eastern end of the basin (Figures 6a and 6b). Our modeling shows that one way to better account for this pattern of uplift and subsidence is to incorporate flexural uplift due to mechanical unloading along the Adventure Fault and the Concordia Fault (Figures 6a and 6b) and high T_e values along the western margin of the WSB (Figure S6).

The original model (ten Brink et al., 1997) is also unable to account for the observed increase in width of the TAM and the WSB in the northern part of the basin and Victoria Land (Figures 6e and 6f). One way in which to account for this widening would be an increase in regional T_e, but to match the observed width of the TAM and WSB here would require unrealistically large values (>120 km) and would stand in stark contrast to values of 40–85 km reported for the WSB (Chen et al., 2017; Ji et al., 2017; ten Brink et al., 1997) and 35 km reported for the continental margin just offshore of the WSB (Close et al., 2009). Instead, the geometry of the TAM and WSB in this area may have been influenced by vertical flexural displacement driven by mechanical unloading along the Rennick Graben (Figures 6e and 6f), the orientation of which mirrors the trend of the underlying architecture of the WSB (Figure 7; Ferraccioli, Armadillo, Jordan, et al., 2009).

Our sensitivity testing shows that the best fitting T_e value for the WSB is ~60 km. The range of permissible values around this best fit is approximately ±25 km, because the pattern of flexure is relatively insensitive to T_e at higher values (Figures 7 and 2). Our results indicate that relatively large T_e values (>35 km) are necessary if the WSB was originally a flexural *back-bulge* feature (ten Brink et al., 1997). Lower T_e values produce a better fit with the residual topography along the TAM and the eastern WSB, whereas higher values give a better fit for the western WSB (Figure S6), indicating that T_e increases from east to west into the continental interior.

5. Discussion

5.1. Cenozoic Landscape Evolution Model

5.1.1. Paleocene–Eocene

Our flexural modeling shows that the variations in width, amplitude, and pattern of the 34 Ma paleotopography of the TAM and WSB (Figure 6) cannot be fully accounted for by previously proposed flexural uplift models (Stern & ten Brink, 1989; ten Brink et al., 1997). We have shown that incorporating vertical flexural displacement due to mechanical unloading along the Rennick Graben, Adventure Fault, and Concordia Fault can improve the overall match between the modeled and observed topography (Figure 6). It has also been proposed that the Adventure and Concordia faults are part of a Cenozoic extensional corridor within East Antarctica (Cianfarra et al., 2009; Cianfarra & Salvini, 2016); coeval uplift along these faults and in Victoria Land (Lisker & Läufer, 2013; Prenzel et al., 2018) during the Paleocene–Oligocene may therefore have initiated the formation of the modern topographic configuration of the TAM and WSB (Figure 8).

Significant discrepancies remain, however, between the observed geometry of the TAM and WSB and the flexural models (Figure 6). One explanation may be lateral variability in the magnitude of thermal and erosional unloading along the edge of the TAM, as is indicated by seismic tomography (Brenn et al., 2017) and apatite fission track thermochronology (Fitzgerald, 2002), and/or lateral variations in T_e. Moreover, flexural uplift due to mechanical unloading during extension in the Ross Sea, which may have played a significant

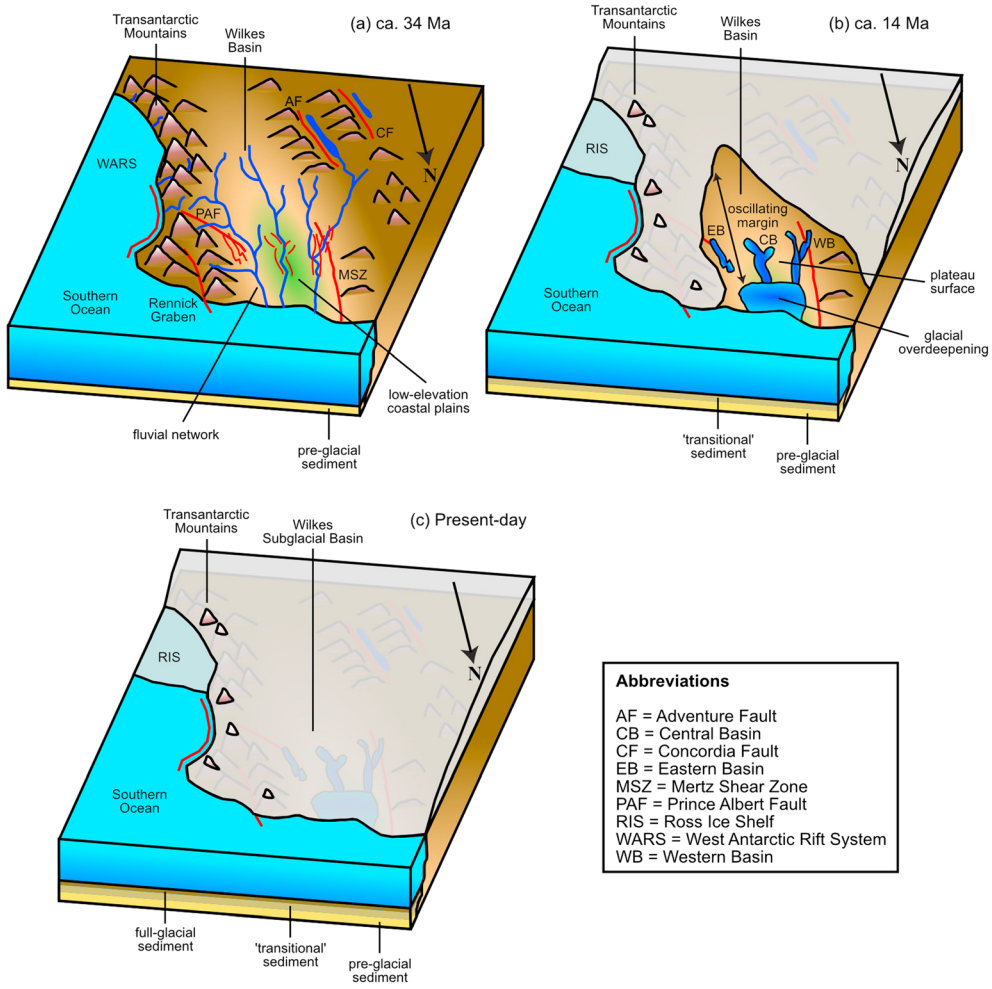

Figure 8. Schematic diagram showing the landscape evolution of the Wilkes Subglacial Basin and Transantarctic Mountains. (a) Prior to East Antarctic Ice Sheet inception at 34 Ma, the Wilkes Subglacial Basin (WSB) region was situated close to sea level, with vegetated low-lying plains being drained by continental river networks, which exploited the existing fault systems (red lines). The Transantarctic Mountains were flexurally uplifted along the flank of the West Antarctic Rift System during the Eocene and dissected by river systems. The geometry of the Transantarctic Mountains and WSB was controlled by inherited fault systems on the eastern and western margins. (b) During the Oligocene–Miocene, the northern WSB was overdeepened by oscillatory and erosive ice sheets, which deposited large volumes of sediment offshore. The inherited tectonic structure and river networks of the basin controlled the location of glacial overdeepening. The remnant bedrock plateaus between the overdeepened basins were flexurally uplifted due to erosional unloading. (c) Since the mid-Miocene climatic optimum (approximately 14 Ma), decreasing surface temperatures allowed full expansion of the East Antarctic Ice Sheet. Bedrock erosion rates decreased, and large regions of the bed were protected beneath cold-based ice.

role in driving TAM uplift during the Cretaceous (Wannamaker et al., 2017), is not included in the original models beyond the simplified *isostatic end load* (ten Brink et al., 1997). We suggest that more detailed determination of the 3-D geometry of extensional, thermal, and erosional (un)loads at the front of the TAM, and the associated flexural responses, is required to fully quantify the role of flexure in the origin of the TAM and WSB. The TAM and elevated hinterland are up to 500 km wide in northern Victoria Land and close to the South Pole, which is difficult to reconcile with a flexural model in which unloading is focused along the edge of the TAM, even for a highly rigid lithosphere. Seismic tomography indicates foundering of the lithosphere beneath the southern TAM and (at least partial) support of the broad, high-elevation hinterland plateau by incursion of buoyant asthenospheric mantle (Shen et al., 2017). The contributions of thermal, tectonic, and mantle dynamic processes to the regional elevation of the mountain range therefore also require more detailed investigation.

Our 34 Ma paleotopography reconstruction shows that the peaks of the TAM were ~800 m lower in the Late Eocene than at present (Figure 5). The early TAM were dissected by river systems (Figure 8), the geomorphic remnants of which are observed within the Dry Valleys (Sugden et al., 1995). The landscape of the northern WSB at 34 Ma was that of a low-relief region situated within 100 m of sea level and bounded by highlands to the east and west. Extensive, flat-lying bedrock plateau surfaces beneath the EAIS are observed in radargrams over the northern WSB and are interpreted as remnants of this low-lying coastal plain formed by fluvial erosion close to sea level (Paxman et al., 2018). These plains, analogous to those observed along the conjugate South Australian margin (Quigley et al., 2010; Sandiford et al., 2009), would have likely hosted major continental river networks, brackish marshes and swamps, and shallow inland seas (Figure 8). If sedimentary basins existed in the vicinity of the modern-day TAM between the Permian and Eocene, as is indicated by thermochronological data (Lisker & Läufer, 2013; Prenzel et al., 2018), the TAM were likely situated at relatively low elevations during much of the Mesozoic, and we note the possibility that some of these cover rocks persisted into the early Oligocene.

5.1.2. Oligocene–Holocene

Following glacial inception at 34 Ma, erosion beneath the early EAIS was controlled by the inherited structure of the WSB. The early ice sheets were likely steered along existing fault-controlled topographic depressions and/or structural weaknesses in the bedrock (Bingham et al., 2012), which had likely also been exploited by preglacial river networks (Figure 8). These regions—the Eastern, Central, and Western Basins—were selectively eroded and overdeepened beneath the EAIS (Figure S7). The majority (~70%) of glacial sedimentation and erosion (and resulting flexural isostatic adjustment) occurred between 34 and 14 Ma (Figure 4), and comparatively little (~30%) landscape change has occurred since 14 Ma (Figure 5). The rate of glacial erosion and sedimentation prior to 14 Ma was approximately double the rate after 14 Ma, assuming that the rate of sediment loss from the shelf has been constant over time. Since the offshore sedimentary record contains several unconformities (Escutia et al., 2011), this assumption is likely to be oversimplistic. However, this scenario, showing a marked slow-down in source-area erosion rates at approximately 14 Ma, closely matches the history of erosion and isostatic uplift in the Lambert Graben region, where it is further constrained by geological evidence (uplifted Oligocene-Neogene fjordal sediments), thermochronology, and flexural models (Hambrey et al., 2007; Hambrey & McKelvey, 2000; Paxman et al., 2016; Thomson et al., 2013; Tochilin et al., 2012).

Glacial incision into basement in the TAM has driven 600–900 m of flexural uplift of the mountain peaks since 34 Ma, assuming that the peaks themselves have not experienced significant denudation over this time. Using thermochronology data sets, it has been proposed that the TAM region was buried beneath 2–4 km of post-Jurassic overburden, which has subsequently been removed (Lisker et al., 2014; Lisker & Läufer, 2013; Prenzel et al., 2018). While the presence of erosion of a spatially uniform overburden would not drive differential peak uplift, this scenario does have implications for the paleo-elevations of the TAM. However, the mass balance between our post-34 Ma onshore erosion estimates and offshore sediments is in close agreement when basement incision alone is considered. This indicates that erosion of any post-Jurassic overburden largely occurred prior to glaciation at 34 Ma, and this process therefore does not influence our Oligocene-Pliocene topographic reconstructions.

Comparisons between our estimated onshore glacial erosion and the observed mass of post-34 Ma offshore sediments indicate that the mass of eroded material routed through the TAM and deposited in the Ross Sea exceeds the mass of post-34 Ma sediment, whereas the reverse is true for the Wilkes Land margin. While each mass balance is associated with uncertainties, this discrepancy may, in part, reflect transport of material by westward flowing ocean currents. Alternatively, it may be that during the early stages of glaciation in the Oligocene, before large outlet glaciers had fully breached through the TAM, more material from the western side of the TAM was routed through the WSB. Drainage analysis indicates a reversal of the Byrd and Beardmore drainage systems in the central TAM after glaciation (Huerta, 2007), suggesting that the drainage divide has shifted north and westward since 34 Ma to its present-day position (Figure 4).

Together, the total amount of glacial valley incision (Figure 3) and offshore sedimentary records (Figure 4) imply long-term average vertical erosion rates beneath the outlet glaciers of 0.04–0.07 mm/year between 34 and 14 Ma and 0.02–0.04 mm/year after 14 Ma. These values are consistent with estimates from the Recovery Catchment (Paxman et al., 2017) and observed erosion rates beneath modern polar glaciers (Koppes et al., 2015). The change in erosion rates likely reflects the change in basal ice dynamics associated with the

expansion of the EAIS after the mid-Miocene climatic optimum and the establishment of polar conditions and cold-based nonerosive ice across large parts of East Antarctica (Sugden et al., 1995). Additionally, erosion rates may have slowed if relatively erodible Cenozoic sedimentary material and graben infill within the Eastern, Central, and Western Basins were removed first, and then the underlying—more consolidated—Beacon sandstones and/or Ferrar dolerites became exposed.

Because the TAM and WSB are long wavelength (~10^3 km) features of Earth's surface topography, the landscape evolution of this part of interior East Antarctica may have been influenced by changes to normal tractions applied to the base of the lithosphere by viscous mantle flow (dynamic topography). However, the magnitude of these changes is still poorly known, because of the uncertainties in seismic tomographic models in Antarctica, which largely result from sparse seismic station coverage (An et al., 2015). There are therefore large uncertainties associated with the mantle convection simulations used to estimate past and present dynamic topography, and we therefore do not attempt to reconstruct these changes here. However, the subglacial geomorphology of the WSB (Paxman et al., 2018) and palynological proxies (Sangiorgi et al., 2018) both indicate that the WSB was situated at low elevations near sea level throughout the late Eocene, Oligocene, and Miocene. Our reconstructions produce a paleotopography (Figure 5) that is in close agreement with a paleo-landscape of this type, without the need to infer major secular change in dynamic topography throughout the Oligocene–Neogene. We note, however, that recent dynamic topography models predict that the bedrock on the western and northern margins of the WSB has been dynamically uplifted by ~100–200 m since the mid-Pliocene (Figure S9; Austermann et al., 2015).

5.2. Implications for Past Ice Sheet Dynamics

Given the slow-down in glacial erosion rates after 14 Ma, most of the overdeepening of the Eastern, Central, and Western Basins occurred in the Oligocene to early Miocene (Figure 8). During this time, the EAIS was likely fluctuating in extent and eroding the landscape as it advanced and retreated across the northern WSB (as has been proposed for the Lambert Graben; Hambrey et al., 2007; Hambrey & McKelvey, 2000; Thomson et al., 2013). The presence of oscillatory and erosive ice sheets between 34 and 14 Ma, which were strongly sensitive to climate forcing, has also been inferred in the Aurora Subglacial Basin, where inland fjord systems associated with a dynamic early EAIS have been described (Aitken et al., 2016; Young et al., 2011). Oscillatory behavior of the EAIS during warm periods of the Miocene is supported by ice sheet model results (Gasson et al., 2016), and the age and provenance of terrigenous sediment on the Wilkes Land margin (Pierce et al., 2017). In addition, terrestrial palynomorphs and soil material in offshore sediment cores indicate the presence of temperate vegetation in the absence of ice near the WSB coast during the mid-Miocene climatic optimum (Sangiorgi et al., 2018). The geometry of the sub-basins within the WSB is not consistent with formation beneath the modern-day EAIS; they are situated ~300 km inland of the enhanced ice flow near the modern grounding zone, and ice surface velocities above the sub-basins are relatively slow (<25 m/year; Figure 1). They therefore likely also date from the time of the early, dynamic ice sheets of the Oligocene-Miocene (Figure 8).

In the WSB, glacial erosion has been controlled by the underlying architecture of the basin. The early ice sheets were likely directed along existing fault-controlled topographic depressions and/or structural weaknesses in the bedrock. These regions were selectively eroded and overdeepened, and bedrock erosion rates increased, driving a positive feedback of selectively enhanced glacial flow and erosion. The removal of eroded material would have driven flexural uplift of the plateau surfaces situated in between the troughs (Paxman et al., 2018) As the relief evolved, more ice would be drained from the plateaus into the outlet glaciers, thereby thinning the ice at higher elevations and lowering subglacial temperatures, preserving the plateau surfaces beneath cold-based ice. Since 14 Ma and the inferred expansion of a continental-scale, polar EAIS (Sugden et al., 1995), erosion/sedimentation rates have been comparatively low (Figure 4), and relatively little landscape change has occurred (Figures 5 and 8). Although global cooling since 14 Ma led to expansion of the EAIS, the gradual overdeepening below sea level of the bedrock of the northern WSB has likely rendered the overlying EAIS more susceptible to rapid inland retreat in response to ocean forcing than the early ice sheets. These implications may be tested using our paleotopographic reconstructions, which provide new boundary conditions for models of ice sheet initiation and evolution.

6. Conclusions

We draw the following conclusions from this study:

1. Our erosion model shows that ~2×10^{18} kg of material has been removed from the TAM and WSB by glacial incision. This is in close agreement with the mass of post-34 Ma sediment located offshore. The removal of the eroded material has driven on average 600–900 m of uplift along the TAM and 200–300 m of uplift in the WSB.
2. The rate of glacial erosion, as inferred from offshore sediment records, decreased by a factor of ~2 following the mid-Miocene climatic optimum (approximately 14 Ma), confirming the findings of previous studies in other regions of Antarctica (Hambrey & McKelvey, 2000). This indicates that the early EAIS was more dynamic and erosive, an interpretation which is supported by geomorphological evidence in the WSB and other subglacial basins around the EAIS margin (Aitken et al., 2016; Young et al., 2011).
3. The regional paleotopography at 34 Ma was characterized by an elevated (but less heavily dissected) TAM, and an extensive, low-relief WSB with bedrock elevations close to sea level. This scenario is supported by independent evidence from vegetation records within offshore sediment cores (Sangiorgi et al., 2018) and the subglacial geomorphology preserved beneath the modern EAIS (Paxman et al., 2018). The dynamics of the early EAIS situated on this paleotopography would likely differ significantly from those at the present day.
4. The 2-D flexural model of ten Brink et al. (1997) cannot alone account for the full 3-D topographic character of both the TAM and WSB. Quantifying the 3-D geometry of the driving (un)loads and associated flexural responses, as well as explicitly incorporating processes such as mechanical unloading due to Ross Sea extension, will facilitate a rigorous assessment of the role of flexure in the origin of the TAM and WSB. For example, our modified flexure model can better account for the overall regional topography of the WSB and TAM by incorporating displacements along additional major fault systems, including those flanking the Rennick Graben and the western margin of the WSB, and by employing a spatially variable Earth model where T_e increases westward across the TAM and WSB to values of up to ~60 km.

Acknowledgments

G. J. G. P. is in receipt of a Natural Environment Research Council UK studentship NE/L002590/1. G. L. acknowledges the support from Russian Science Foundation grant 16-17-10139. We would like to thank Garry Karner, Frank Lisker, and an anonymous reviewer for their thorough and constructive reviews. Grids and figures were produced using the Generic Mapping Tools (GMT) software package (Wessel et al., 2013). MATLAB scripts used to numerically calculate flexure on a plate with spatially variable rigidity are freely downloadable at http://www.ux.uis.no/~nestor/work/matlabScripts.html. ICECAP and Operation IceBridge data products used in this study are available through the Icebridge data portal at the National Snow and Ice Data Center (http://nsdic.org/icebridge/portal/). The processed WISE-ISODYN radar data are freely available on the NERC/BAS Polar Data Centre airborne geophysics data portal (https://doi.org/10.5285/59e5a6f5-e67d-4a05-99af-30f656569401). This paper is UTIG contribution 3032. Reconstructed topography grids produced as part of this study are available to download in the supplementary information.

References

Aitken, A. R. A., Roberts, J. L., van Ommen, T. D., Young, D. A., Golledge, N. R., Greenbaum, J. S., et al. (2016). Repeated large-scale retreat and advance of Totten Glacier indicated by inland bed erosion. *Nature*, *533*(7603), 385–389. https://doi.org/10.1038/nature17447

Aitken, A. R. A., Young, D. A., Ferraccioli, F., Betts, P. G., Greenbaum, J. S., Richter, T. G., et al. (2014). The subglacial geology of Wilkes Land, East Antarctica. *Geophysical Research Letters*, *41*, 2390–2400. https://doi.org/10.1002/2014GL059405

An, M., Wiens, D. A., Zhao, Y., Feng, M., Nyblade, A. A., Kanao, M., et al. (2015). S-velocity model and inferred Moho topography beneath the Antarctic Plate from Rayleigh waves. *Journal of Geophysical Research: Solid Earth*, *120*, 359–383. https://doi.org/10.1002/2014JB011332

Austermann, J., Pollard, D., Mitrovica, J. X., Moucha, R., Forte, A. M., DeConto, R. M., et al. (2015). The impact of dynamic topography change on Antarctic ice sheet stability during the mid-Pliocene warm period. *Geology*, *43*(10), 927–930. https://doi.org/10.1130/G36988.1

Bamber, J. L., Riva, R. E. M., Vermeersen, B. L. A., & LeBrocq, A. M. (2009). Reassessment of the potential sea-level rise from a collapse of the West Antarctic Ice Sheet. *Science*, *324*(5929), 901–903. https://doi.org/10.1126/science.1169335

Bingham, R. G., Ferraccioli, F., King, E. C., Larter, R. D., Pritchard, H. D., Smith, A. M., & Vaughan, D. G. (2012). Inland thinning of West Antarctic Ice Sheet steered along subglacial rifts. *Nature*, *487*(7408), 468–471. https://doi.org/10.1038/nature11292

Blankenship, D. D., Kempf, S. D., & Young, D. A. (2017). *IceBridge HiCARS 1 L2 Geolocated Ice Thickness, Version 1*. Boulder, Colorado USA: NASA National Snow and Ice Data Center Distributed Active Archive Center.

Brenn, G. R., Hansen, S. E., & Park, Y. (2017). Variable thermal loading and flexural uplift along the Transantarctic Mountains, Antarctica. *Geology*, *45*(5), 463–466. https://doi.org/10.1130/G38784.1

Champagnac, J. D., Molnar, P., Anderson, R. S., Sue, C., & Delacou, B. (2007). Quaternary erosion-induced isostatic rebound in the western Alps. *Geology*, *35*(3), 195–198. https://doi.org/10.1130/G23053A.1

Chen, B., Haeger, C., Kaban, M. K., & Petrunin, A. G. (2017). Variations of the effective elastic thickness reveal tectonic fragmentation of the Antarctic lithosphere. *Tectonophysics*, *746*, 412–424. https://doi.org/10.1016/j.tecto.2017.06.012

Chiappini, M., Ferraccioli, F., Bozzo, E., & Damaske, D. (2002). Regional compilation and analysis of aeromagnetic anomalies for the Transantarctic Mountains-Ross Sea sector of the Antarctic. *Tectonophysics*, *347*(1–3), 121–137. https://doi.org/10.1016/S0040-1951(01)00241-4

Cianfarra, P., Forieri, A., Salvini, F., Tabacco, I. E., & Zirizotti, A. (2009). Geological setting of the Concordia Trench-Lake system in East Antarctica. *Geophysical Journal International*, *177*(3), 1305–1314. https://doi.org/10.1111/j.1365-246X.2009.04123.x

Cianfarra, P., & Salvini, F. (2014). Ice sheet surface lineaments as nonconventional indicators of East Antarctica bedrock tectonics. *Geosphere*, *10*(6), 1411–1418. https://doi.org/10.1130/GES01074.1

Cianfarra, P., & Salvini, F. (2016). Origin of the Adventure Subglacial Trench linked to Cenozoic extension in the East Antarctic Craton. *Tectonophysics*, *670*, 30–37. https://doi.org/10.1016/j.tecto.2015.12.011

Close, D. I., Watts, A. B., & Stagg, H. M. J. (2009). A marine geophysical study of the Wilkes Land rifted continental margin, Antarctica. *Geophysical Journal International*, *177*(2), 430–450. https://doi.org/10.1111/j.1365-246X.2008.04066.x

Cook, C. P., Van De Flierdt, T., Williams, T., Hemming, S. R., Iwai, M., Kobayashi, M., et al. (2013). Dynamic behaviour of the East Antarctic Ice Sheet during Pliocene warmth. *Nature Geoscience*, *6*(9), 765–769. https://doi.org/10.1038/ngeo1889

DeConto, R. M., & Pollard, D. (2016). Contribution of Antarctica to past and future sea-level rise. *Nature*, *531*(7596), 591–597. https://doi.org/10.1038/nature17145

Escutia, C., Brinkhuis, H., & Klaus, A. (2011). IODP Expedition 318: From greenhouse to icehouse at the Wilkes Land Antarctic Margin. *Scientific Drilling*, *12*(12, September 2011), 15–23. https://doi.org/10.2204/iodp.sd.12.02.2011

Ferraccioli, F., Armadillo, E., Jordan, T., Bozzo, E., & Corr, H. (2009). Aeromagnetic exploration over the East Antarctic Ice Sheet: A new view of the Wilkes Subglacial Basin. *Tectonophysics*, *478*(1–2), 62–77. https://doi.org/10.1016/j.tecto.2009.03.013

Ferraccioli, F., Armadillo, E., Zunino, A., Bozzo, E., Rocchi, S., & Armienti, P. (2009). Magmatic and tectonic patterns over the Northern Victoria Land sector of the Transantarctic Mountains from new aeromagnetic imaging. *Tectonophysics*, *478*(1–2), 43–61. https://doi.org/10.1016/j.tecto.2008.11.028

Ferraccioli, F., & Bozzo, E. (2003). Cenozoic strike-slip faulting from the eastern margin of the Wilkes Subglacial Basin to the western margin of the Ross Sea Rift: An aeromagnetic connection. *Geological Society, London, Special Publications*, *210*(1), 109–133. https://doi.org/10.1144/GSL.SP.2003.210.01.07

Fitzgerald, P. G. (1992). The Transantarctic Mountains of Southern Victoria Land: The application of apatite fission track analysis to a rift shoulder uplift. *Tectonics*, *11*(3), 634–662. https://doi.org/10.1029/91TC02495

Fitzgerald, P. G. (2002). Tectonics and landscape evolution of the Antarctic plate since the breakup of Gondwana, with an emphasis on the West Antarctic Rift System and the Transantarctic Mountains. *Royal Society of New Zealand Bulletin*, *35*, 453–469.

Frederick, B. C., Young, D. A., Blankenship, D. D., Richter, T. G., Kempf, S. D., Ferraccioli, F., & Siegert, M. J. (2016). Distribution of subglacial sediments across the Wilkes Subglacial Basin, East Antarctica. *Journal of Geophysical Research: Earth Surface*, *121*, 790–813. https://doi.org/10.1002/2015JF003760

Fretwell, P., Pritchard, H. D., Vaughan, D. G., Bamber, J. L., Barrand, N. E., Bell, R., et al. (2013). Bedmap2: Improved ice bed, surface and thickness datasets for Antarctica. *The Cryosphere*, *7*(1), 375–393. https://doi.org/10.5194/tc-7-375-2013

Gasson, E., DeConto, R. M., & Pollard, D. (2015). Antarctic bedrock topography uncertainty and ice sheet stability. *Geophysical Research Letters*, *42*, 5372–5377. https://doi.org/10.1002/2015GL064322

Gasson, E., DeConto, R. M., Pollard, D., & Levy, R. H. (2016). Dynamic Antarctic ice sheet during the early to mid-Miocene. *Proceedings of the National Academy of Sciences*, *113*(13), 3459–3464. https://doi.org/10.1073/pnas.1516130113

Golledge, N. R., Levy, R. H., McKay, R. M., & Naish, T. R. (2017). East Antarctic Ice Sheet most vulnerable to Weddell Sea warming. *Geophysical Research Letters*, *44*, 2343–2351. https://doi.org/10.1002/2016GL072422

Hambrey, M. J., Glasser, N., McKelvey, B., Sugden, D., & Fink, D. (2007). Cenozoic landscape evolution of an East Antarctic oasis (Radok Lake area, northern Prince Charles Mountains), and its implications for the glacial and climatic history of Antarctica. *Quaternary Science Reviews*, *26*(5–6), 598–626. https://doi.org/10.1016/j.quascirev.2006.11.014

Hambrey, M. J., & McKelvey, B. (2000). Major Neogene fluctuations of the East Antarctic Ice Sheet: Stratigraphic evidence from the Lambert Glacier region. *Geology*, *28*(10), 887–890. https://doi.org/10.1130/0091-7613(2000)28<887:MNFOTE>2.0.CO;2

Hansen, S. E., Kenyon, L. M., Graw, J. H., Park, Y., & Nyblade, A. A. (2016). Crustal structure beneath the Northern Transantarctic Mountains and Wilkes Subglacial Basin: Implications for tectonic origins. *Journal of Geophysical Research: Solid Earth*, *121*, 812–825. https://doi.org/10.1002/2015JB012325

Huerta, A. D. (2007) 'Byrd drainage system; evidence of a Mesozoic West Antarctic plateau', in Cooper, A. K. and Raymond, C. R. (eds) *Antarctica: A Keystone in a changing World – Online Proceedings of the 10th ISAES X: USGS Open-File Report 2007-1047*, p. Extended Abstract 091, 5 p.

Jamieson, S. S. R., Stokes, C. R., Ross, N., Rippin, D. M., Bingham, R. G., Wilson, D. S., et al. (2014). The glacial geomorphology of the Antarctic ice sheet bed. *Antarctic Science*, *26*(06), 724–741. https://doi.org/10.1017/S0954102014000212

Ji, F., Gao, J., Shen, Z., Zhang, Q., & Li, Y. (2017). Variations of the effective elastic thickness over the Ross Sea and Transantarctic Mountains and implications for their structure and tectonics. *Tectonophysics*, *717*, 127–138. https://doi.org/10.1016/j.tecto.2017.07.011

Jordan, T. A., Ferraccioli, F., Armadillo, E., & Bozzo, E. (2013). Crustal architecture of the Wilkes Subglacial Basin in East Antarctica, as revealed from airborne gravity data. *Tectonophysics*, *585*, 196–206. https://doi.org/10.1016/j.tecto.2012.06.041

Jordan, T. A., Ferraccioli, F., Corr, H., Graham, A., Armadillo, E., & Bozzo, E. (2010). Hypothesis for mega-outburst flooding from a palaeo-subglacial lake beneath the East Antarctic Ice Sheet. *Terra Nova*, *22*(4), 283–289. https://doi.org/10.1111/j.1365-3121.2010.00944.x

Jordan, T. A., Ferraccioli, F., Vaughan, D. G., Holt, J. W., Corr, H., Blankenship, D. D., & Diehl, T. M. (2010). Aerogravity evidence for major crustal thinning under the Pine Island Glacier region (West Antarctica). *Bulletin of the Geological Society of America*, *122*(5–6), 714–726. https://doi.org/10.1130/B26417.1

Koppes, M., Hallet, B., Rignot, E., Mouginot, J., Wellner, J. S., & Boldt, K. (2015). Observed latitudinal variations in erosion as a function of glacier dynamics. *Nature*, *526*(7571), 100–103. https://doi.org/10.1038/nature15385

Lawrence, J. F., Wiens, D. A., Nyblade, A. A., Anandakrishnan, S., Shore, P. J., & Voigt, D. (2006). Crust and upper mantle structure of the transantarctic mountains and surrounding regions from receiver functions, surface waves, and gravity: Implications for uplift models. *Geochemistry, Geophysics, Geosystems*, *7*, Q10011. https://doi.org/10.1029/2006GC001282

Leuschen, C., Gogineni, P., Rodriguez-Morales, F., Paden, J., & Allen, C. (2016). *IceBridge MCoRDS L2 Ice Thickness, Version 1*. Boulder, Colorado USA: NASA National Snow and Ice Data Center Distributed Active Archive Center.

Lindeque, A., Gohl, K., Wobbe, F., & Uenzelmann-Neben, G. (2016). Preglacial to glacial sediment thickness grids for the Southern Pacific Margin of West Antarctica. *Geochemistry, Geophysics, Geosystems*, *17*, 4276–4285. https://doi.org/10.1002/2016GC006401

Lisker, F. (2002). Review of fission track studies in northern Victoria Land, Antarctica—Passive margin evolution versus uplift of the Transantarctic Mountains. *Tectonophysics*, *349*(1–4), 57–73. https://doi.org/10.1016/S0040-1951(02)00046-X

Lisker, F., & Läufer, A. L. (2013). The Mesozoic Victoria Basin: Vanished link between Antarctica and Australia. *Geology*, *41*(10), 1043–1046. https://doi.org/10.1130/G33409.1

Lisker, F., Prenzel, J., Läufer, A. L., & Spiegel, C. (2014). Recent thermochronological research in Northern Victoria Land, Antarctica. *Polarforschung*, *84*, 59–66.

Mengel, M., & Levermann, A. (2014). Ice plug prevents irreversible discharge from East Antarctica. *Nature Climate Change*, *4*(6), 451–455. https://doi.org/10.1038/nclimate2226

Mercer, J. H. (1978). West Antarctic ice sheet and CO2 greenhouse effect: A threat of disaster. *Nature*, *104*(25), 10,335–10,339. https://doi.org/10.1073/pnas.0703993104

Molnar, P., & England, P. (1990). Late Cenozoic uplift of mountain ranges and global climate change: Chicken or egg? *Nature*, *346*(6279), 29–34. https://doi.org/10.1038/346029a0

ten Brink, U. S., Hackney, R. I., Bannister, S., Stern, T. A., & Makovsky, Y. (1997). Uplift of the Transantarctic Mountains and the bedrock beneath the East Antarctic Ice Sheet. *Journal of Geophysical Research*, *102*(B12), 27,603–27,621. https://doi.org/10.1029/97jb02483

Naish, T., Powell, R., Levy, R., Wilson, G., Scherer, R., Talarico, F., et al. (2009). Obliquity-paced Pliocene West Antarctic ice sheet oscillations. *Nature*, *458*(7236), 322–328. https://doi.org/10.1038/nature07867

Naish, T. R., Woolfe, K. J., Barrett, P. J., Wilson, G. S., Atkins, C., Bohaty, S. M., et al. (2001). Orbitally induced oscillations in the East Antarctic Ice Sheet at the Oligocene/Miocene boundary. *Nature*, *413*(6857), 719–723. https://doi.org/10.1038/35099534

Paxman, G. J. G., Jamieson, S. S. R., Ferraccioli, F., Bentley, M. J., Forsberg, R., Ross, N., et al. (2017). Uplift and tilting of the Shackleton Range in East Antarctica driven by glacial erosion and normal faulting. *Journal of Geophysical Research: Solid Earth*, *122*, 2390–2408. https://doi.org/10.1002/2016JB013841

Paxman, G. J. G., Jamieson, S. S. R., Ferraccioli, F., Bentley, M. J., Ross, N., Armadillo, E., et al. (2018). Bedrock erosion surfaces record former East Antarctic Ice Sheet extent. *Geophysical Research Letters*, *45*, 4114–4123. https://doi.org/10.1029/2018GL077268

Paxman, G. J. G., Watts, A. B., Ferraccioli, F., Jordan, T. A., Bell, R. E., Jamieson, S. S. R., & Finn, C. A. (2016). Erosion-driven uplift in the Gamburtsev Subglacial Mountains of East Antarctica. *Earth and Planetary Science Letters*, *452*, 1–14. https://doi.org/10.1016/j.epsl.2016.07.040

Pierce, E. L., van de Flierdt, T., Williams, T., Hemming, S. R., Cook, C. P., & Passchier, S. (2017). Evidence for a dynamic East Antarctic Ice Sheet during the mid-Miocene climate transition. *Earth and Planetary Science Letters*, *478*, 1–13. https://doi.org/10.1016/j.epsl.2017.08.011

Pollard, D., DeConto, R. M., & Alley, R. B. (2015). Potential Antarctic ice sheet retreat driven by hydrofracturing and ice cliff failure. *Earth and Planetary Science Letters*, *412*, 112–121. https://doi.org/10.1016/j.epsl.2014.12.035

Prenzel, J., Lisker, F., Monsees, N., Balestrieri, M. L., Läufer, A., & Spiegel, C. (2018). Development and inversion of the Mesozoic Victoria Basin in the Terra Nova Bay (Transantarctic Mountains) derived from thermochronological data. *Gondwana Research. International Association for Gondwana Research*, *53*, 110–128. https://doi.org/10.1016/j.gr.2017.04.025

Quigley, M. C., Clark, D., & Sandiford, M. (2010). Tectonic geomorphology of Australia. *Geological Society, London, Special Publications*, *346*(1), 243–265. https://doi.org/10.1144/SP346.13

Rignot, E., Jacobs, S., Mouginot, J., & Scheuchl, B. (2013). Ice-shelf melting around Antarctica. *Science*, *341*(6143), 266–270. https://doi.org/10.1126/science.1235798

Rignot, E., Mouginot, J., & Scheuchl, B. (2011). Ice flow of the Antarctic Ice Sheet. *Science*, *333*(6048), 1427–1430. https://doi.org/10.1126/science.1208336

Sandiford, M., Quigley, M., de Broekert, P., & Jakica, S. (2009). Tectonic framework for the Cenozoic cratonic basins of Australia. *Australian Journal of Earth Sciences*, *56*(sup1), S5–S18. https://doi.org/10.1080/08120090902870764

Sangiorgi, F., Bijl, P. K., Passchier, S., Salzmann, U., Schouten, S., McKay, R., et al. (2018). Southern Ocean warming and Wilkes Land ice sheet retreat during the mid-Miocene. *Nature Communications*. Springer US, *9*(1), 317–311. https://doi.org/10.1038/s41467-017-02609-7

Scheinert, M., Ferraccioli, F., Schwabe, J., Bell, R., Studinger, M., Damaske, D., et al. (2016). New Antarctic gravity anomaly grid for enhanced geodetic and geophysical studies in Antarctica. *Geophysical Research Letters*, *43*, 600–610. https://doi.org/10.1002/2015GL067439

Schoof, C. (2007). Ice sheet grounding line dynamics: Steady states, stability, and hysteresis. *Journal of Geophysical Research*, *112*, F03S28. https://doi.org/10.1029/2006JF000664

Shen, W., Wiens, D. A., Stern, T., Anandakrishnan, S., Aster, R. C., Dalziel, I., et al. (2017). Seismic evidence for lithospheric foundering beneath the southern Transantarctic Mountains, Antarctica. *Geology*, *46*(1), 71–74. https://doi.org/10.1130/G39555.1

Siegert, M. J., Taylor, J., & Payne, A. J. (2005). Spectral roughness of subglacial topography and implications for former ice-sheet dynamics in East Antarctica. *Global and Planetary Change*, *45*(1-3), 249–263. https://doi.org/10.1016/j.gloplacha.2004.09.008

Stern, T. A., Baxter, A. K., & Barrett, P. J. (2005). Isostatic rebound due to glacial erosion within the Transantarctic Mountains. *Geology*, *33*(3), 221–224. https://doi.org/10.1130/G21068.1

Stern, T. A., & ten Brink, U. S. (1989). Flexural uplift of the Transantarctic Mountains. *Journal of Geophysical Research*, *94*(B8), 10,315–10,330. https://doi.org/10.1029/JB094iB08p10315

Studinger, M., Bell, R. E., Buck, W. R., Karner, G. D., & Blankenship, D. D. (2004). Sub-ice geology inland of the Transantarctic Mountains in light of new aerogeophysical data. *Earth and Planetary Science Letters*, *220*(3–4), 391–408. https://doi.org/10.1016/S0012-821X(04)00066-4

Sugden, D. E., Denton, G. H., & Marchant, D. R. (1995). Landscape evolution of the Dry Valleys, Transantarctic Mountains: Tectonic implications. *Journal of Geophysical Research*, *100*(B6), 9949–9968. https://doi.org/10.1029/94JB02875

Tauxe, L., Stickley, C. E., Sugisaki, S., Bijl, P. K., Bohaty, S. M., Brinkhuis, H., et al. (2012). Chronostratigraphic framework for the IODP Expedition 318 cores from the Wilkes Land Margin: Constraints for paleoceanographic reconstruction. *Paleoceanography*, *27*, PA2214. https://doi.org/10.1029/2012PA002308

Thomson, S. N., Reiners, P. W., Hemming, S. R., & Gehrels, G. E. (2013). The contribution of glacial erosion to shaping the hidden landscape of East Antarctica. *Nature Geoscience*, *6*(3), 203–207. https://doi.org/10.1038/ngeo1722

Tochilin, C. J., Reiners, P. W., Thomson, S. N., Gehrels, G. E., Hemming, S. R., & Pierce, E. L. (2012). Erosional history of the Prydz Bay sector of East Antarctica from detrital apatite and zircon geo- and thermochronology multidating. *Geochemistry, Geophysics, Geosystems*, *13*, Q11015. https://doi.org/10.1029/2012GC004364

Wannamaker, P., Hill, G., Stodt, J., Maris, V., Ogawa, Y., Selway, K., et al. (2017). Uplift of the Central Transantarctic Mountains. *Nature Communications*, *8*(1), 1588. https://doi.org/10.1038/s41467-017-01577-2

Watts, A. B. (2001). *Isostasy and flexure of the lithosphere*. Cambridge: Cambridge University Press.

Weissel, J. K., & Karner, G. D. (1989). Flexural uplift of rift flanks due to mechanical unloading of the lithosphere during extension. *Journal of Geophysical Research*, *94*(B10), 13,919–13,950. https://doi.org/10.1029/JB094iB10p13919

Wessel, P., Smith, W. H. F., Scharroo, R., Luis, J., & Wobbe, F. (2013). Generic Mapping Tools: Improved version released. *Eos, Transactions American Geophysical Union*, *94*(45), 409–410. https://doi.org/10.1002/2013EO450001

Wilson, D. S., Jamieson, S. S. R., Barrett, P. J., Leitchenkov, G., Gohl, K., & Larter, R. D. (2012). Antarctic topography at the Eocene-Oligocene boundary. *Palaeogeography, Palaeoclimatology, Palaeoecology*, *335-336*, 24–34. https://doi.org/10.1016/j.palaeo.2011.05.028

Wilson, D. S., Pollard, D., DeConto, R. M., Jamieson, S. S. R., & Luyendyk, B. P. (2013). Initiation of the West Antarctic Ice Sheet and estimates of total Antarctic ice volume in the earliest Oligocene. *Geophysical Research Letters*, *40*, 4305–4309. https://doi.org/10.1002/grl.50797

Young, D. A., Wright, A. P., Roberts, J. L., Warner, R. C., Young, N. W., Greenbaum, J. S., et al. (2011). A dynamic early East Antarctic Ice Sheet suggested by ice-covered fjord landscapes. *Nature*, *474*(7349), 72–75. https://doi.org/10.1038/nature10114

Zattin, M., Andreucci, B., Thomson, S. N., Reiners, P. W., & Talarico, F. M. (2012). New constraints on the provenance of the ANDRILL AND-2A succession (western Ross Sea, Antarctica) from apatite triple dating. *Geochemistry, Geophysics, Geosystems*, *13*, Q10016. https://doi.org/10.1029/2012GC004357